catalysts

*Article*

# Oxygen Vacancy-Mediated Selective $H_2S$ Oxidation over Co-Doped $LaFe_xCo_{1-x}O_3$ Perovskite

**Xinlei Yu [1], Xun Tao [1], Yunfei Gao [1,*], Lu Ding [1], Yanqin Wang [2], Guangsuo Yu [1] and Fuchen Wang [1,*]**

[1] Shanghai Engineering Research Center of Coal Gasification, East China University of Science and Technology, Shanghai 200237, China; y20160073@mail.ecust.edu.cn (X.Y.); taoxun@mail.ecust.edu.cn (X.T.); dinglu@ecust.edu.cn (L.D.); gsyu@ecust.edu.cn (G.Y.)
[2] Research Institute of Industrial Catalysis, School of Chemistry and Molecular Engineering, East China University of Science and Technology, Shanghai 200237, China; wangyanqin@ecust.edu.cn
* Correspondence: yunfeigao@ecust.edu.cn (Y.G.); wfch@ecust.edu.cn (F.W.)

**Abstract:** Compared to the Claus process, selective $H_2S$ catalytic oxidation to sulfur is a promising reaction, as it is not subject to thermodynamic limitations and could theoretically achieve ~100% $H_2S$ conversion to sulfur. In this study, we investigated the effects of Co and Fe co-doping in $ABO_3$ perovskite on $H_2S$ selective catalytic oxidation. A series of $LaFe_xCo_{1-x}O_3$ (x = 0, 0.2, 0.4, 0.6, 0.8, 1.0) perovskites were synthesized by the sol-gel method. Compared to $LaFeO_3$ and $LaCoO_3$, co-doped $LaFe_xCo_{1-x}O_3$ significantly improved the $H_2S$ conversion and sulfur selectivity at a lower reaction temperature. Nearly 100% sulfur yield was achieved on $LaFe_{0.4}Co_{0.6}O_3$ under 220 °C with exceptional catalyst stability (above 95% sulfur yield after 77 h). The catalysts were characterized by XRD, BET, FTIR, XPS, and $H_2$-TPR. The characterization results showed that the structure of $LaFe_xCo_{1-x}O_3$ changed from the rhombic phase of $LaCoO_3$ to the cubic phase of $LaFeO_3$ with Fe substitution. Doping with appropriate iron (x = 0.4) facilitates the reduction of Co ions in the catalyst, thereby promoting the $H_2S$ selective oxidation. This study demonstrates a promising approach for low-temperature $H_2S$ combustion with ~100% sulfur yield.

**Keywords:** hydrogen sulfide; selective oxidation; perovskite oxides; oxygen vacancy



**Citation:** Yu, X.; Tao, X.; Gao, Y.; Ding, L.; Wang, Y.; Yu, G.; Wang, F. Oxygen Vacancy-Mediated Selective $H_2S$ Oxidation over Co-Doped $LaFe_xCo_{1-x}O_3$ Perovskite. *Catalysts* **2022**, *12*, 236. https://doi.org/10.3390/catal12020236

Academic Editors: Baiqian Dai, Xiaojiang Wu and Lian Zhang

Received: 17 January 2022
Accepted: 9 February 2022
Published: 19 February 2022



## 1. Introduction

Natural gas processing/utilizing processes, petroleum refining processes, and coal chemistry produce $H_2S$-containing waste gas [1–3].The removal of $H_2S$ from industry waste gas is crucial as $H_2S$ is a toxic and corrosive gas, leading to severe pollution and equipment/pipeline corrosion [4]. Numerous efforts have been conducted to remove $H_2S$ and the most widely used technology is called the Claus process, which recovers elemental sulfur from $H_2S$-containing gas [5,6]. However, due to thermodynamic limitations, the Claus process cannot achieve 100% $H_2S$ conversion, leaving 2–5% unconverted $H_2S$ gas remaining after the treatment [7]. Selective $H_2S$ catalytic oxidation could be added as a secondary process after the Claus process apparatus to oxidize the residual, low-concentration $H_2S$-containing gas to elemental sulfur with increased overall sulfur yield. The design of a catalyst with high $H_2S$ conversion and high sulfur selectivity is the key to the selective catalytic oxidation. So far, $H_2S$ selective oxidation catalysts mainly include active carbon (AC)-based catalysts [8], carbon nanotube-based catalysts [9], clay-supported catalysts [10], and metal oxide-based catalysts [11]. Nevertheless, most of these $H_2S$ selective oxidation catalysts face challenge on the needs of excessive oxygen feed, which is produced from economically expensive air separation units. For instance, Fang et al. [8] found that the Mn/AC catalyst can achieve optimal catalytic activity at 180 °C, but it needs excess amounts of oxygen to participate in the $H_2S$ oxidation process. Ba et al. [9] found that the $H_2S$ conversion over nitrogen-doped carbon nanotubes dropped from 100% to 92% as the $O_2/H_2S$ ratio decreased from 2.5 to 0.6. Soriano et al. [11] observed that VNa-0.1 had

high sulfur selectivity at 200 °C under the $H_2S$/air/He molar ratio of 1.2/5.0/93.8, with an excess of $O_2$. Moreover, the durations of the catalyst stability in the literature were usually not long, less than 20 h [12–14]. Thus, a catalyst with remarkable catalytic activity, excellent selectivity, outstanding stability, and desired stoichiometric $H_2S/O_2$ operating conditions is urgently needed.

Perovskite oxides such as $ABO_3$ have been extensively investigated. The typical structure of perovskite oxides is cubic, with one A-site cation coordinated by 12 anions and eight B-site cations (belonging to 1/8 to one specific unit cell) coordinated by six anions [15,16]. For (distorted) perovskites with lower symmetry, the first shell coordination numbers are smaller. It is well-recognized that the tuning of A and B site cations can affect the catalytic activity and stability of perovskite oxides. Moreover, structural modifications related to the generation of the oxygen vacancies and/or changes in the valence states of the original cations can be achieved by the partial substitution of the ions at A site or B site [17–19]. Therefore, the flexibility and chemical versatility of $ABO_3$ perovskite oxides can be used to design highly active, selective, and stable catalysts [20]. Among these, $LaCoO_3$ and $LaFeO_3$ stand out as redox catalysts with satisfactory catalytic performance reported for CO oxidation [21] and NO oxidation [22]. Moreover, Yang et al. [23] found that $LaCoO_3$ showed high $H_2S$ conversion and high selectivity to sulfur (98.2%) at 260 °C. Zhang et al. [24] found that $LaFeO_3$ exhibited outstanding selectivity (100%) under relatively low reaction temperature and various $H_2S/O_2$ ratios. It is desired to obtain catalysts with ~100% $H_2S$ conversion and ~100% sulfur selectivity, and the influence of co-doping Fe and Co into the B-site of perovskite could be further explored.

This work investigates the influence of Fe substitution on $LaCoO_3$ in $H_2S$ selective oxidation. $LaFe_xCo_{1-x}O_3$ (x = 0, 0.2, 0.4, 0.6, 0.8, 1) perovskite oxides were synthesized by the sol-gel method and their catalytic behaviors in the $H_2S$ selective oxidation were investigated. It was observed that the incorporation of iron enhanced the catalytic activity of the $LaFe_xCo_{1-x}O_3$ catalysts. In addition, the crystal structure and redox ability were comprehensively investigated by various characterization techniques such as XRD, BET, FTIR, XPS, and $H_2$-TPR. On the basis of these results, the catalytic and deactivation mechanisms of $H_2S$ selective oxidation over $LaFe_xCo_{1-x}O_3$ are discussed.

## 2. Experiment

### *2.1. Catalyst Preparation*

Powder samples of $LaFe_xCo_{1-x}O_3$ (x = 0, 0.2, 0.4, 0.6, 0.8, and 1.0) perovskite oxides were synthesized by the sol-gel method using citric acid as a complexing agent. The starting materials were $La(NO_3)_3{\cdot}6H_2O$ (AR, Macklin, Shanghai, China), $Fe(NO_3)_3{\cdot}9H_2O$ (AR, Macklin, Shanghai, China), and $Co(NO_3)_2{\cdot}6H_2O$ (AR, Macklin, Shanghai, China). The required amounts of nitrate samples were first dissolved in distilled water. Citric acid (AR, Aladdin, Shanghai, China) was added so that the number of moles of citric acid was equal to the number of moles of total metal cations. The obtained solution was evaporated at 80 °C and then PEG-20000 (AR, Macklin, Shanghai, China) was added into the solution. Stirring was continued until a viscous gel was formed. Finally, the gel was dried in an oven at 105 °C overnight and calcined at 650 °C for 5 h in a furnace to obtain the catalyst samples.

### *2.2. Catalyst Characterization*

XRD (X-ray diffraction) patterns were determined using the X'Pert PRO powder diffraction system (Empyrean, San Jose, California, USA) with Cu Kα radiation (λ = 0.15418 nm, 40 kV/40 mA) in the 2$\theta$ range of 10–80°.

BET (Brunauer–Emmett–Teller) surface areas and textural properties of the catalysts were determined by nitrogen adsorption–desorption isotherms using an ASAP-2020 apparatus (Micromeritics, Norcross, GA, USA). The adsorption process was carried out at liquid nitrogen temperature. The BET method was adopted to calculate the specific surface area.

FTIR (Fourier transform infrared) spectra were measured using a Nicolet Model iS-50 instrument (Thermo Scientific, Waltham, MA, USA) in the region from 400 to 4000 $cm^{-1}$. The sample was taken in pellet form in the KBr matrix for measurement.

X-ray photoelectron spectroscopy (XPS) was performed on an ESCALAB 250Xi (Thermo Scientific, USA) with Al Kα radiation as the radiation source at 300 W. The spectra of C 1s, O 1s, La 3d, Co 2p, and Fe 2p were recorded. The binding energies were calibrated using the C 1s peak of contaminant carbon (B.E. = 284.8 eV) as the standard.

$H_2$-TPR ($H_2$ temperature-programmed reduction) experiment was measured on an Auto Chem 2920 chemical adsorption instrument (Micromeritics, Norcross, GA, USA). The TPR profiles were obtained by passing a 10% $H_2$/Ar flow (50 mL/min) through the pretreated catalyst (about 60 mg). The temperature was increased from room temperature to 700 °C with a rate of 10 °C/min, and the $H_2$ concentration was measured by a thermal conductivity detector. Before the determination, the catalyst was heated to 300 °C under He atmosphere for 60 min.

### *2.3. Catalytic Performance Tests*

All catalytic tests were performed in a continuous flow fixed-bed quartz reactor with an internal diameter of 10 mm at atmospheric pressure, as shown in Figure 1. A certain amount of catalyst was placed in the reactor. A simulant gas was flown into the reactor, with 0.5% $H_2S$, 0.25% $O_2$, and balance gas of $N_2$. The total gas flow rate was fixed at 150 mL/min and the reaction temperature ranged from 180 °C to 260 °C. A sulfur condenser was attached to the bottom of the fixed-bed quartz reactor. The tail gas was analyzed by gas chromatography (GC2060, Ruimin, China) equipped with an FPD (flame photometric detector) and a TCD (thermal conductivity detector). We note that in $H_2S$ oxidation, the formation of S is considered a selective reaction and the formation of $SO_2$ is considered an unselective reaction. The conversion of $H_2S$, sulfur selectivity, and sulfur yield were determined by the following equations:

$$H_2S\ \text{conversion}(\%) = \frac{[H_2S]_{in} - [H_2S]_{out}}{[H_2S]_{in}} \times 100\% \quad (1)$$

$$\text{Sulfur selectivity}(\%) = \frac{[H_2S]_{in} - [H_2S]_{out} - [SO_2]_{out}}{[H_2S]_{in} - [H_2S]_{out}} \times 100\% \quad (2)$$

$$\text{Sulfur yield}(\%) = [H_2S\ \text{conversion}] \times [\text{sulfur selectivity}] \times 100\% \quad (3)$$

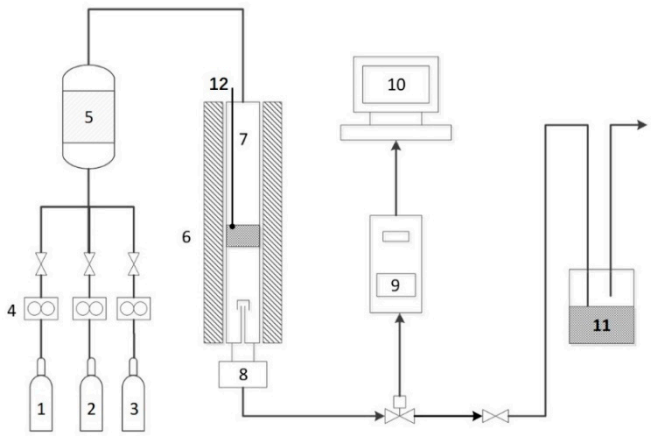


**Figure 1.** Schematic diagram of $H_2S$ catalytic process: (1) 1% $H_2S$ gas cylinder; (2) $N_2$ gas cylinder; (3)$O_2$ gas cylinder; (4) mass flow controllers; (5) gas mixer; (6) tube furnace; (7) fixed bed reactor; (8) condenser; (9) gas chromatograph; (10) computer; (11) NaOH wash bottle; (12) thermocouple.

## 3. Results and Discussion

### *3.1. Catalytic Performances of $LaFe_xCo_{1-x}O_3$ Catalysts*

#### 3.1.1. Effect of Reaction Temperature

The effect of reaction temperature on the catalytic performance of the $LaFe_xCo_{1-x}O_3$ catalysts for $H_2S$ selective catalytic oxidation is investigated in Figure 2. Figure 2A shows the $H_2S$ conversion for $LaCoO_3$, $LaFeO_3$, and Fe-doped $LaCoO_3$. At 180 °C, $LaCoO_3$ can only achieve $H_2S$ conversion of 75%, while $LaFeO_3$ achieved slightly higher $H_2S$ conversion of 83%. With Fe co-doping in the B-site, $H_2S$ conversions were significantly higher, and all samples achieved conversions higher than 88%. This indicates that B-site Fe doping significantly increases the activity of the pristine perovskite catalysts. Temperature effects were also investigated. For $LaCoO_3$, it was shown that $H_2S$ conversion increased with temperature and eventually reached 93% at 260 °C. For co-doped $LaFe_{0.4}Co_{0.6}O_3$, $LaFe_{0.6}Co_{0.4}O_3$, and $LaFe_{0.8}Co_{0.2}O_3$, $H_2S$ conversion increased to 99% at only 200 °C. This again shows that $LaFe_xCo_{1-x}O_3$ with Fe doping has notably higher activities. For $LaFeO_3$, the $H_2S$ conversion increased and then decreased with the further increasing temperature. This could be ascribed to lattice oxygen uncoupling from the perovskite structure at higher temperatures, which caused a loss of activity of perovskite [25].

Figure 2B compares the selectivities towards sulfur. It was observed that $LaFeO_3$ exhibited almost perfect selectivities (~100%) at all temperatures investigated, while $LaCoO_3$ exhibited lower selectivity, with ~95% at 180 °C. A small amount of Fe doping did not increase the selectivity, and 94% sulfur selectivity was achieved for $LaFe_{0.2}Co_{0.8}O_3$ at 180 °C. However, a further increase in Fe contents significantly increased the selectivities, and >98% selectivities were achieved for $LaFe_{0.4}Co_{0.6}O_3$, $LaFe_{0.6}Co_{0.4}O_3$, and $LaFe_{0.2}Co_{0.8}O_3$. This again shows that larger Fe co-doping is beneficial. Temperature effects were also investigated. For $LaCoO_3$ and $LaFe_{0.2}Co_{0.8}O_3$, the selectivities increased with respect to temperature. For $LaFe_{0.4}Co_{0.6}O_3$, $LaFe_{0.6}Co_{0.4}O_3$, and $LaFe_{0.2}Co_{0.8}O_3$, a volcanic shape was present and the highest selectivities (~100%) were obtained at 220 °C. Sulfur yield was further compared in Figure 2C. As expected, $LaFe_{0.4}Co_{0.6}O_3$, $LaFe_{0.6}Co_{0.4}O_3$, and $LaFe_{0.2}Co_{0.8}O_3$ achieved ~100% sulfur yield at 220 °C, higher than $LaFe_{0.2}Co_{0.8}O_3$, $LaFeO_3$, and $LaCoO_3$. This shows that perovskites with Co and Fe co-doping are highly effective in $H_2S$ selective oxidation to sulfur.

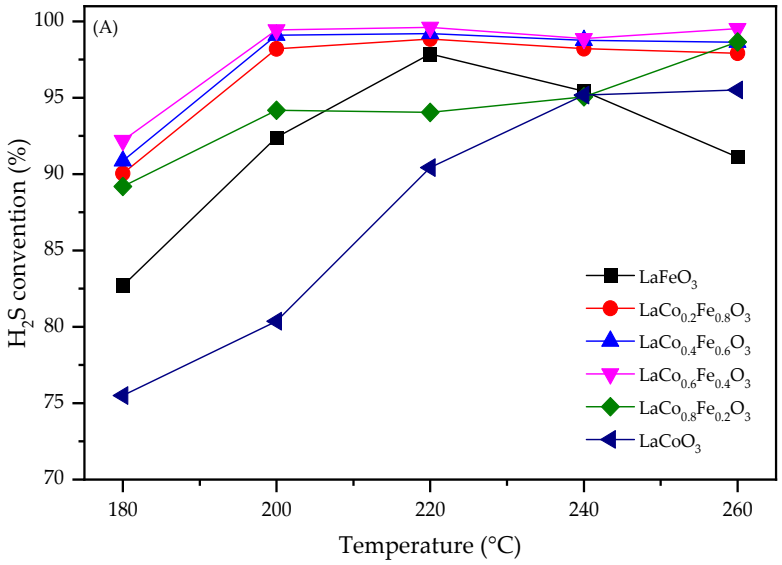


**Figure 2.** *Cont.*

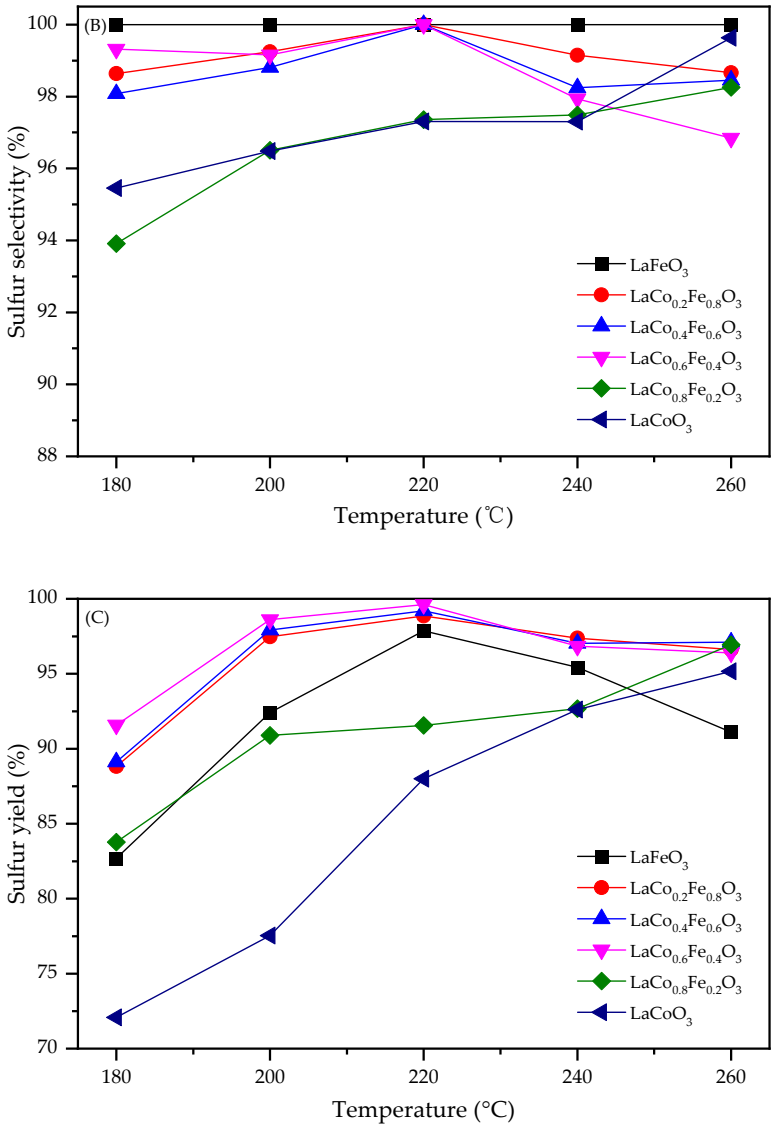


**Figure 2.** Effect of temperature on (**A**) $H_2S$ conversion, (**B**) sulfur selectivity, and (**C**) sulfur yield for $LaFe_xCo_{1-x}O_3$ catalysts.

### 3.1.2. Effect of GHSV (Gas Hourly Space Velocity)

$LaFe_{0.4}Co_{0.6}O_3$ was selected as one of the best catalysts for selective $H_2S$ oxidation. The influence of GHSV on the performance of the $LaFe_{0.4}Co_{0.6}O_3$ catalyst was investigated at 220 °C. As shown in Figure 3, the $H_2S$ conversion, sulfur selectivity, and sulfur yield were all above 99% when the GHSV was in the range of 3000 $h^{-1}$–6000 $h^{-1}$. However, it was found that as the GHSV further increased, the catalytic activity of $LaFe_{0.4}Co_{0.6}O_3$ catalyst was greatly reduced. $H_2S$ conversion decreased from 99% to 82% with the increase in GHSV from 6000 $h^{-1}$ to 15,000 $h^{-1}$. Therefore, $LaFe_{0.4}Co_{0.6}O_3$ presented excellent catalytic performance in the GHSV range of 3000 $h^{-1}$–6000 $h^{-1}$.

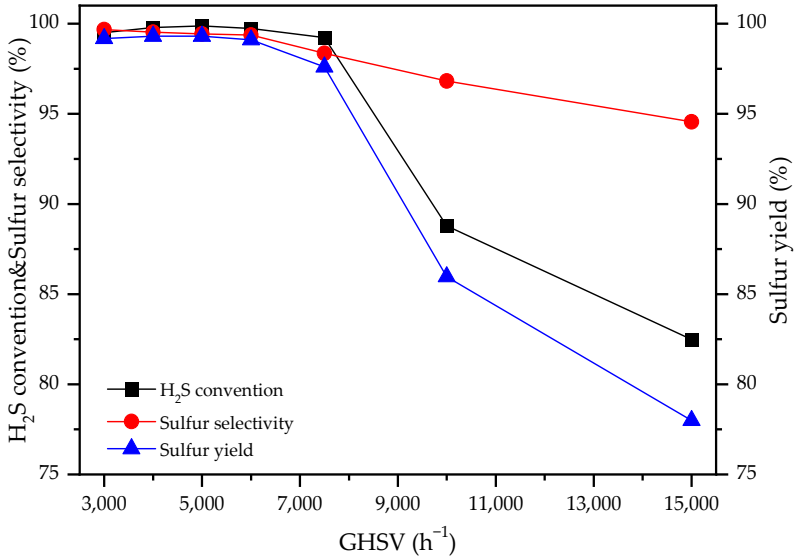


**Figure 3.** Effect of GHSV on catalytic performance for $LaFe_{0.4}Co_{0.6}O_3$ catalysts at 220 °C.

### 3.1.3. Effect of the $H_2S/O_2$ Molar Ratio

Figure 4 depicts the effect of the $H_2S/O_2$ molar ratio on $H_2S$ selective catalytic oxidation over the $LaFe_{0.4}Co_{0.6}O_3$ catalyst at 220 °C. As shown in Figure 4, as the $H_2S/O_2$ molar ratio decreased from 3:1 to 2:1 (i.e., from oxygen-deficient to stoichiometric), $H_2S$ conversion increased from 75% to nearly 100% with sulfur selectivity close to 100%. As $H_2S/O_2$ further reduced to 1 (i.e., oxygen-excess), $H_2S$ conversion decreased slightly, but sulfur selectivity decreased drastically to ~70%. This is attributed to the further oxidation of the generated sulfur to sulfur dioxide under excess oxygen. Therefore, as opposed to previous studies that required an oxygen-excess environment [9,11], co-doped $LaFe_{0.4}Co_{0.6}O_3$ catalyst only requires stoichiometric $H_2S/O_2$ condition, showing process advantages.

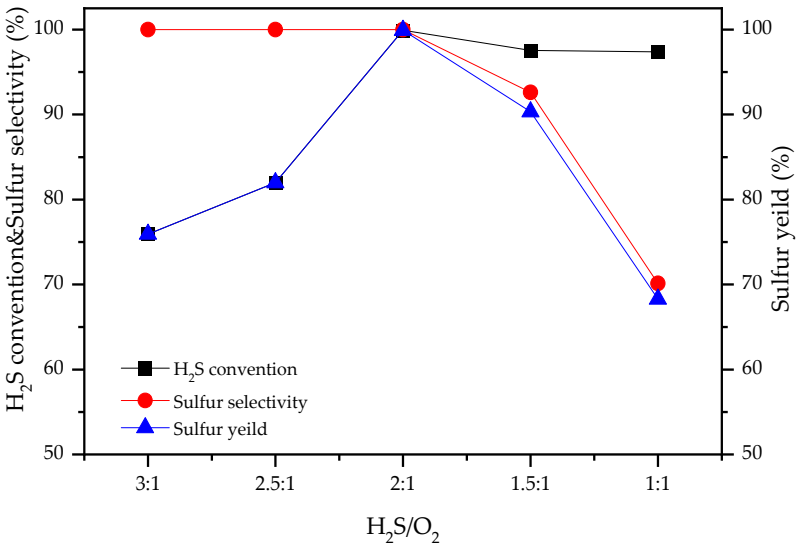


**Figure 4.** Effect of the $H_2S/O_2$ molar ratio on the catalytic performance of $LaFe_{0.4}Co_{0.6}O_3$ catalysts. Reaction conditions: $H_2S/O_2/N_2$ = 0.5/0.25/99.25, T = 220 °C, GHSV = 5000 $h^{-1}$.

### 3.1.4. Durability of $LaFe_xCo_{1-x}O_3$ Catalysts

Catalyst stability is an important criterion for industrial applications. Figure 5 illustrates the durability behavior of the $LaFe_{0.4}Co_{0.6}O_3$ catalyst at 220 °C. The selectivity of sulfur can be maintained at ~100% with the reaction proceeding within 77 h. For catalyst activity, during the first 64 h, the $H_2S$ conversion of the $LaFe_{0.4}Co_{0.6}O_3$ catalyst decreased

slightly from 99.9% to 98.1%. The deactivation accelerated after 64 h; however, $H_2S$ conversion was still above 95% at 77 h. Longer reaction time was not attempted given the limitation of the lab equipment. Although deactivation was still observed, the co-doped $LaFe_{0.4}Co_{0.6}O_3$ catalyst exhibited excellent stability when compared with several other reported catalysts using a 5% decrease in sulfur yield as a criterion. The comparisons with previously reported carbon materials, pillared clay materials, and metal oxides are shown in Figure 6 [2,7,13,26,27].

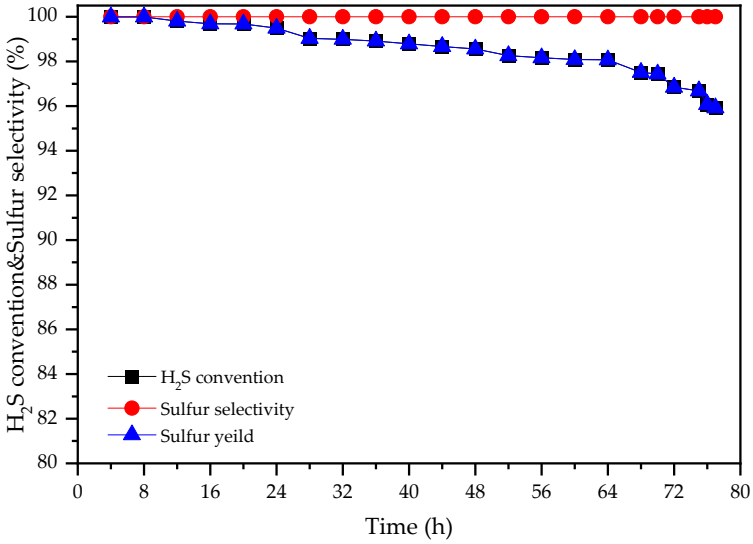


**Figure 5.** Time-on-stream behavior of the $LaFe_{0.4}Co_{0.6}O_3$ catalysts. Reaction conditions: $H_2S/O_2/N_2$ = 0.5/0.25/99.25, T = 220 °C, GHSV = 5000 $h^{-1}$.

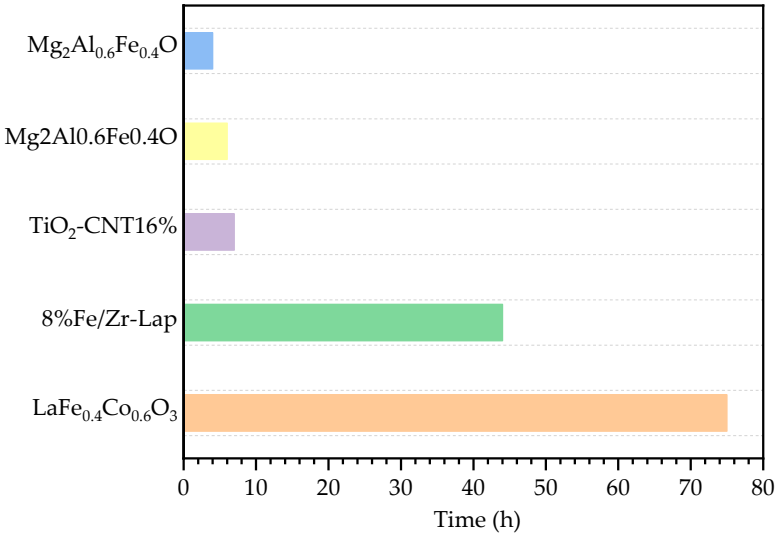


**Figure 6.** Time-on-stream behavior of different catalysts using sulfur yield decreased by 5% as a criterion.

### *3.2. Characterization of $LaFe_xCo_{1-x}O_3$ Catalysts*

#### 3.2.1. Phase Identifications

The phase structures of all catalysts were examined by XRD. Figure 7 shows the XRD patterns of $LaFeO_3$, $LaCoO_3$, and $LaFe_xCo_{1-x}O_3$ catalysts. It was observed that co-doped $LaFe_xCo_{1-x}O_3$ generally maintained a perovskite-phase structure. With increasing amounts of Fe (III) dopant, a small shift to lower 2-theta angles was observed, indicating that $Fe^{3+}$ is substituted into the perovskite structure. For x = 0, 0.2, and 0.4, there is a clear

reflection peak splitting at 59.4°, consistent with the spitting of the main peak at 33°. For x = 0.6 and x = 0.8, the peak splitting effect has become less apparent, but the peak shape is still asymmetric. It is noted that the peak splitting effect is minimal on $LaFeO_3$, with no Co-doping. This behavior is mainly due to the transformation of the phase structure from a rhombohedral structure of $LaCoO_3$ (PDF 84-0848) to a cubic structure of $LaFeO_3$ (PDF 75-0541) with $Fe^{3+}$ dopant.

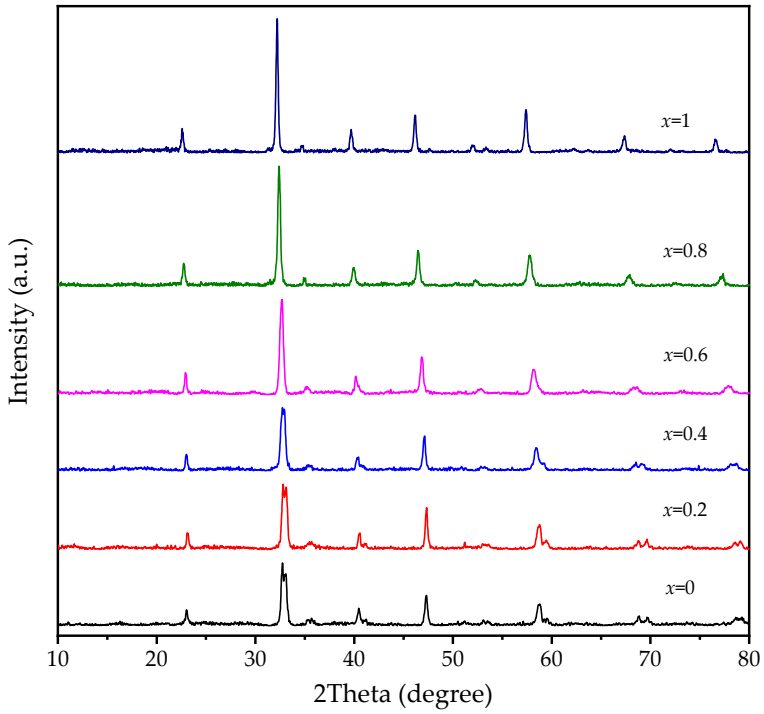


**Figure 7.** XRD patterns of $LaFe_xCo_{1-x}O_3$ catalysts calcined at 650 °C.

### 3.2.2. FTIR Spectrum

FTIR has the advantage of being very sensitive to structural distortions [28]. Figure 8 shows the FTIR spectra of $LaFeO_3$, $LaCoO_3$, and $LaFe_xCo_{1-x}O_3$ catalysts. The ~3400 $cm^{-1}$ band may be the water vapor background error caused by the instrument state. Moreover, the catalysts were calcined at 650 °C and any remaining $CH_X$ shall not appear. $LaCoO_3$ has the characteristic bands at 418 $cm^{-1}$ (stretching La-O vibrations) [29], 553 $cm^{-1}$ (stretching Co-O vibrations) [30], and 595 $cm^{-1}$ (bending O-Co-O vibrations) [31] that ascribed to the vibration of the metal–oxygen band. As a comparison, the FTIR spectrum of $LaFeO_3$ shows stretching Fe–O vibration at 555 $cm^{-1}$, which corresponds to the stretching Fe–O vibration in $FeO_6$ octahedra [32,33]. For $LaFe_xCo_{1-x}O_3$, with the increase in Fe doping, two bands at 553 $cm^{-1}$ and 595 $cm^{-1}$ gradually changed to a single band at 555 $cm^{-1}$, and no new band was found. This indicates that the structure distortion of $LaFe_xCo_{1-x}O_3$ changed from $LaCoO_3$-like to $LaFeO_3$-like with an increasing amount of Fe doping. This result is consistent with XRD.

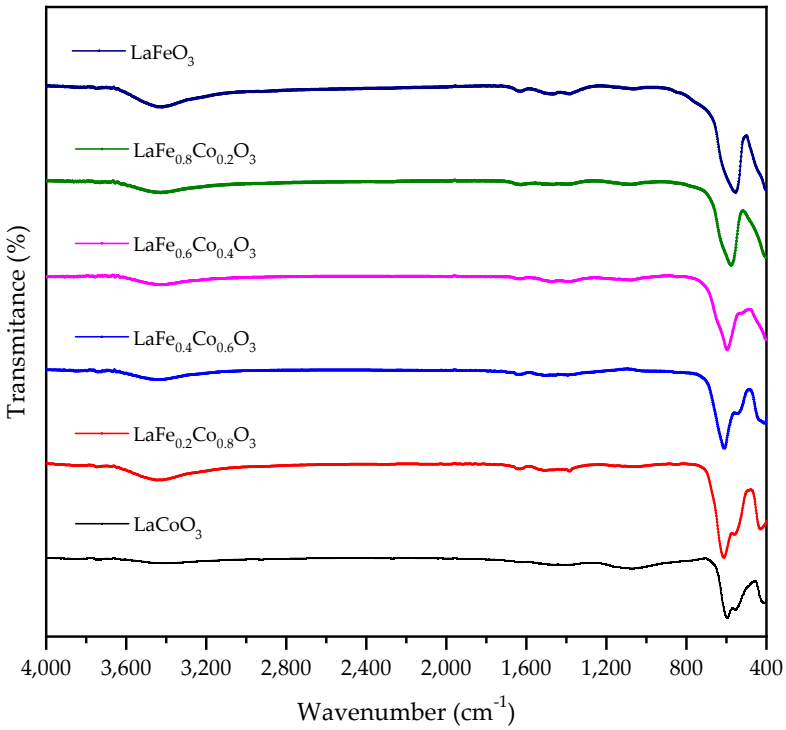


**Figure 8.** FTIR spectra of fresh $LaFe_xCo_{1-x}O_3$ catalysts (x = 0, 0.2, 0.4, 0.6, 0.8, 1.0).

### 3.2.3. Textural Properties

The specific surface area and pore structure of the catalyst were studied by $N_2$-physisorption analysis. Table 1 summarizes the BET surface area, pore volume, and average pore diameter of all investigated catalysts. The specific surface area increased from 9.26 $m^2/g$ of $LaCoO_3$ to 11.39 $m^2/g$ of $LaFe_{0.4}Co_{0.6}O_3$ with the increase in Fe doping amount, and further decreased to 8.02 $m^2/g$ of $LaFeO_3$ with excess Fe in the B-site. This trend is also consistent with the increase in $H_2S$ conversion, indicating that the increasing specific surface area of the catalyst may be favorable for the exposure of active sites, leading to higher catalytic activity [24].

**Table 1.** Textural properties of the $LaFe_xCo_{1-x}O_3$ catalysts.

| Catalysts | BET Surface Area ($S_{BET}$) ($m^2/g$) | Average Pore Diameter ($D_P$) (nm) | Pore Volume ($V_P$) ($cm^3/g$) |
|---|---|---|---|
| $LaCoO_3$ | 9.26 | 20.85 | 0.048 |
| $LaFe_{0.2}Co_{0.8}O_3$ | 10.43 | 18.30 | 0.048 |
| $LaFe_{0.4}Co_{0.6}O_3$ | 11.39 | 19.92 | 0.057 |
| $LaFe_{0.6}Co_{0.4}O_3$ | 10.70 | 20.67 | 0.055 |
| $LaFe_{0.8}Co_{0.2}O_3$ | 9.62 | 22.06 | 0.053 |
| $LaFeO_3$ | 8.02 | 24.22 | 0.049 |

The low temperature data at 180 °C are used to illustrate this effect, as all high temperature points have close to 100% $H_2S$ conversion, which cannot reflect the intrinsic activity of the oxygen vacancies. We set the lowest surface area as 1 and scale other samples based on that. It is shown in Figure 9 that after normalization, except for $LaFeO_3$ and $LaFe_{0.8}Co_{0.2}O_3$, all other samples have similar conversions between 64% and 68%. This reflects that the intrinsic nature of oxygen vacancies is similar and a larger surface area with more oxygen vacancies exposed can lead to higher catalyst activity. This is consistent with the conclusion of this manuscript, where oxygen vacancy is an important factor to determine catalyst activity. As for the increased intrinsic activity of oxygen vacancies for $LaFeO_3$ and $LaFe_{0.8}Co_{0.2}O_3$, this could be due to Fe-enriched perovskite having oxygen

vacancies with higher activity. It would be an interesting topic in the future to synthesize Fe-enriched perovskite with higher surface areas to further boost catalyst activity.

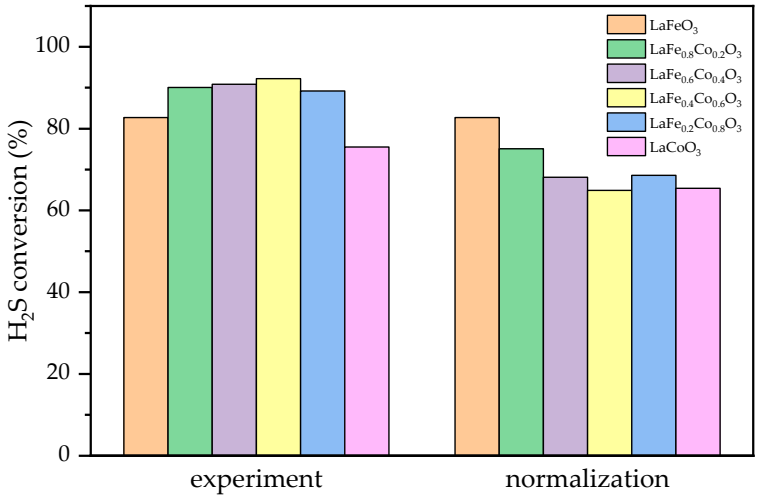


**Figure 9.** Experimental and normalized $H_2S$ conversion of $LaFe_xCo_{1-x}O_3$ catalysts at 180 °C.

### 3.2.4. $H_2$-TPR Spectrum

$H_2$-TPR was conducted to determine the reducibility of the catalysts, as shown in Figure 10. It can be seen that the $LaCoO_3$ sample has reduction peaks at 380 °C and 405 °C, which can be attributed to the reduction of $Co^{3+}$ to $Co^{2+}$ [34], and a higher-temperature reduction peak at 546 °C belonging to the reduction of $Co^{2+}$ to $Co^0$ [35,36]. The addition of Fe in the $LaCoO_3$ leads to reduction peaks with lower temperatures. For example, $LaFe_{0.2}Co_{0.8}O_3$ catalyst has reduction peaks at 367 °C and 390 °C. With the further increase in the Fe doping amount, $LaFe_{0.4}Co_{0.6}O_3$, $LaFe_{0.6}Co_{0.4}O_3$, $LaFe_{0.8}Co_{0.2}O_3$, and $LaFeO_3$ show reduction peaks in the range of 300 °C–400 °C. These indicate that the addition of Fe promotes the reduction of $Co^{3+}$. As the reduction of $Co^{3+}$ to $Co^{2+}$ is also associated with the creation of lattice oxygen vacancies, it can be concluded that Co and Fe co-doping facilitates oxygen vacancy formation in perovskite. This is consistent with the trend of $H_2S$ conversion, which indicates that the ease of oxygen vacancy formation leads to increased catalyst activities for $H_2S$ oxidation. This result is also consistent with other literature reports [37,38]. The high-temperature reduction peak (546 °C in $LaCoO_3$) was pushed to a much higher temperature (660 °C in $LaFe_{0.2}Co_{0.8}O_3$), and completely eliminated in $LaFe_{0.4}Co_{0.6}O_3$, $LaFe_{0.6}Co_{0.4}O_3$, and $LaFe_{0.8}Co_{0.2}O_3$ [39,40]. The higher-temperature reduction peak is associated with further $Co^{2+}$ reduction to $Co^0$, which indicates that the Co and Fe co-doped samples are highly stable even under a high-temperature reducing environment, explaining the exceptional catalyst stability observed in experiments. The reduction peak area also increased with the increase in Fe doping amount, which also indicates that Fe-doped $LaCoO_3$ has stronger oxidation ability and a higher amount of active lattice oxygen [41].

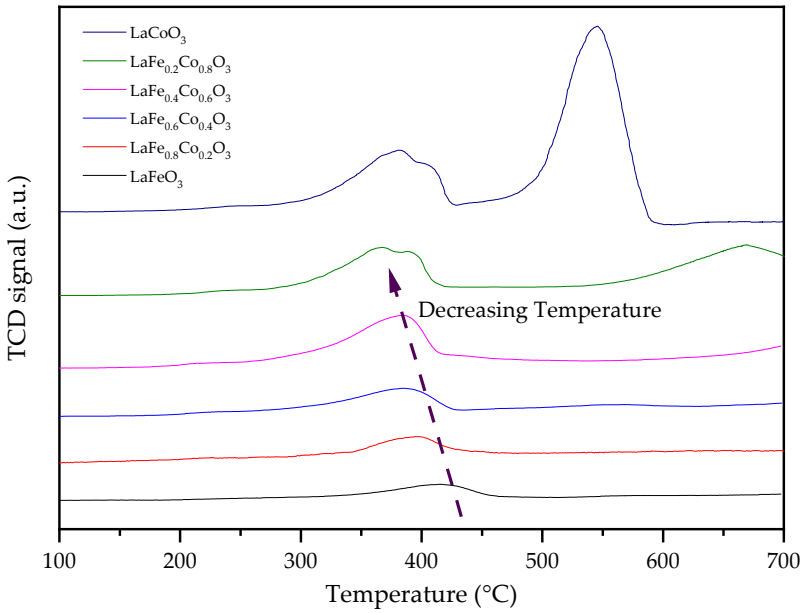


**Figure 10.** $H_2$-TPR patterns of $LaFe_xCo_{1-x}O_3$ catalysts calcined at 650 °C.

3.2.5. The Surface Chemical States Revealed by XPS

XPS analysis was conducted to elucidate the chemical states of surface Co, Fe, O, and S species of the fresh and used $LaFe_{0.4}Co_{0.6}O_3$ catalysts, shown in Figure 11. From the high-resolution spectrum of Co 2p (Figure 11a), it can be seen that there are peaks at bonding energies of 795.1 eV and 780.0 eV, corresponding to $2p_{1/2}$ and $2p_{3/2}$ of $Co^{3+}$, respectively [42–44]. Two peaks appeared at 710.4 eV and 723.8 eV in Figure 11b and can be ascribed to Fe $2p_{3/2}$ and Fe $2p_{1/2}$ levels, respectively. These binding energies agreed well with an $Fe^{3+}$ oxidation state assignment [45,46]. The O 1s spectrum was shown in Figure 11c, which showed two peaks at 531.2 eV and 529.0 eV. The peak at 529.0 eV is attributed to lattice oxygen ($O_{lat}$), while the peak at 531.2 eV corresponds to adsorbed oxygen ($O_{ads}$) on oxygen vacancies [42,47,48]. It was reported that oxygen vacancy plays an important role in the reaction, and can not only accelerate the decomposition of oxygen molecules, but also increase the mobility of lattice oxygen [49]. It can be seen that the content of lattice oxygen decreased sharply, which confirms that the lattice oxygen of the catalyst may participate in the $H_2S$ oxidation reaction to form sulfate species. Simultaneously, the oxygen peaks were shifted towards higher B.E., with a shift value of 0.3 eV and 0.9 eV for lattice oxygen species and oxygen vacancies. As a shift to higher B.E. indicates lower electron density, this shows that the oxygen vacancies in used samples have much lower electron density. It was reported that oxygen vacancies with lower electron density lead to significantly lower ethylene yield in oxidative dehydrogenation of ethane [50]. The shift could also be caused by the formation of $OH^-$ and $SO_4^{2-}$ groups during the catalytic reaction. In this study, it is hypothesized that the deactivation of the $H_2S$ selective oxidation reaction is also mainly related to the lower electron density of oxygen vacancies. Figure 11d shows the S 2p XPS spectrum of the used $LaFe_{0.4}Co_{0.6}O_3$ catalyst to investigate the deactivation process of the catalyst. Tiny peaks around 163.3 eV were detected, which can be ascribed to the presence of the conjugated sulfur ($S_n$) [51], indicating a sulfur deposit on the sample. The main peaks of S $2p_{1/2}$ and S $2p_{3/2}$ at binding energies of 170.3 eV and 169.0 eV indicate that S exists as a sulfate species [52]. It should be noted that deposited sulfur could also lead to catalyst deactivations.

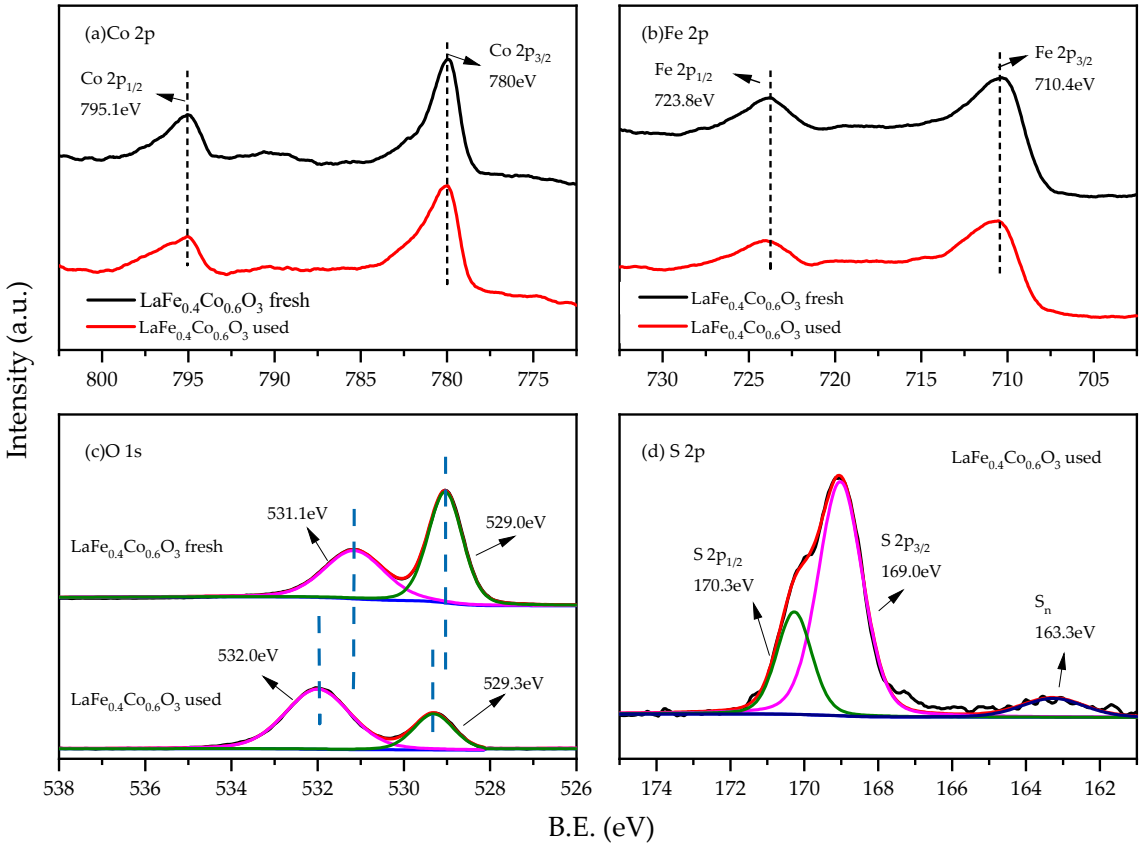


**Figure 11.** XPS spectra of the fresh and used $LaFe_{0.4}Co_{0.6}O_3$ catalysts calcined at 650 °C. (**a**) Co 2p (**b**) Fe 2p (**c**) S 1s (**d**) S 2p.

### *3.3. Catalytic and Deactivation Mechanisms*

Based on the results of experiments and characterizations, the possible reaction mechanism of $H_2S$ selective oxidation over $LaFe_{0.4}Co_{0.6}O_3$ can be proposed as follows: $H_2S$ was first adsorbed on the oxygen vacancies on the $LaFe_{0.4}Co_{0.6}O_3$ catalyst surface, then the adsorbed $H_2S$ dissociated into $HS^-$ or $S^{2-}$ ions. Subsequently, the $HS^-$ or $S^{2-}$ ions were oxidized by the surface-active oxygen and/or lattice oxygen of the $LaFe_{0.4}Co_{0.6}O_3$ catalyst, and $Fe^{3+}$ was reduced to $Fe^{2+}$ or $Co^{3+}$ to $Co^{2+}$ and oxygen vacancies were formed. Then, $O_2$ diffused and adsorbed on the catalyst surfaces, and oxidized $Fe^{2+}$ to $Fe^{3+}$ or $Co^{2+}$ to $Co^{3+}$, thereby replenishing the lattice oxygen. The possible reaction mechanism of $H_2S$ selective oxidation over the $LaFe_{0.4}Co_{0.6}O_3$ is proposed as illustrated in Figure 12. Compared to $LaFeO_3$ and $LaCoO_3$, co-doped $LaFe_{0.4}Co_{0.6}O_3$ has high oxygen vacancy concentration, leading to increased catalyst activities.

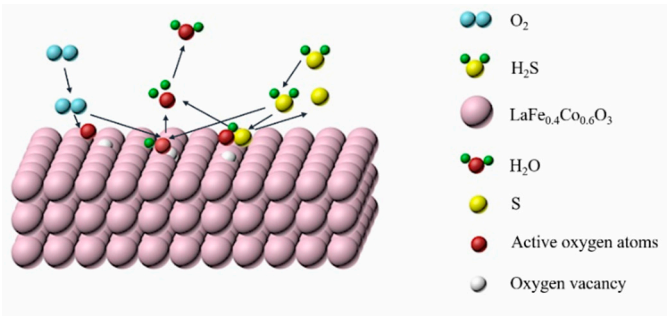


**Figure 12.** Schematic of $H_2S$ selective oxidation over the $LaFe_{0.4}Co_{0.6}O_3$.

The S 2p XPS spectrum of used $LaFe_{0.4}Co_{0.6}O_3$ revealed the deactivation process of the catalyst. The sulfate accounted for 92% of the total molar amount of sulfur and the

elemental sulfur accounted for 8%. The Fe 2p energy value of the used catalyst shifted slightly to a higher value, an index of an increase in positive polarity, indicating that the interaction between sulfate anion and iron cation generates $Fe_2(SO_4)_3$ [24]. It can be concluded that the catalyst deactivation is mainly due to the formation of iron sulfate, which will destroy the redox process of $Fe^{3+}/Fe^{2+}$, resulting in a decrease in catalytic activity. The deposition of elemental sulfur also leads to a reduction in catalytic activity.

## 4. Conclusions

In summary, a series of $LaFe_xCo_{1-x}O_3$ catalysts were synthesized by the sol-gel method and investigated for $H_2S$ selective oxidation. XRD, $N_2$-adsorption, $H_2$-TPR, and XPS analyses were conducted. The conclusions of this study can be summarized as follows:

(1) The incorporation of Fe into $LaCoO_3$ had a great influence on the conversion and selectivity of $H_2S$ selective oxidation reaction. It was shown that Fe doping not only enhanced catalytic activity for the $H_2S$ selective oxidation reaction, but also reduced the optimal reaction temperature.

(2) $LaFe_{0.4}Co_{0.6}O_3$ had the highest catalytic activity and the catalyst deactivation was not obvious before 77 h, and its stability is better than some types of catalysts. Analysis of XRD and FTIR showed that the $LaFe_xCo_{1-x}O_3$ catalyst existed in a single perovskite structure. $H_2$-TPR indicates that oxygen vacancy creation is more feasible on a co-doped $LaFe_xCo_{1-x}O_3$ catalyst.

(3) The reaction mechanism and inactivation mechanism were predicted. The presence of lattice oxygen in the $LaFe_{0.4}Co_{0.6}O_3$ catalyst and the oxygen vacancies generated in the reaction are beneficial to the $H_2S$ selective oxidation reaction. In addition, the deposition of elemental sulfur and the formation of oxygen vacancies with lower electron density could lead to catalyst deactivation.

**Author Contributions:** Conceptualization, X.Y., Y.G. and F.W.; formal analysis, X.Y. and X.T.; investigation, X.Y., X.T. and Y.G.; data curation, X.Y.; writing—original draft preparation, X.Y.; writing—review and editing, Y.G., L.D. and Y.W.; supervision, G.Y.; project administration, F.W.; funding acquisition, F.W. All authors have read and agreed to the published version of the manuscript.

**Funding:** This research was funded by the National Natural Science Foundation of China, grant number 21978092.

**Institutional Review Board Statement:** Not applicable.

**Data Availability Statement:** The data presented in this study are available in this paper.

**Conflicts of Interest:** The authors declare no conflict of interest.

**Sample Availability:** Samples of the compounds $LaFe_xCo_{1-x}O_3$ are available from the authors per requested.

## References

1. Pongthawornsakun, B.; Phatyenchuen, S.; Panpranot, J.; Praserthdam, P. The low temperature selective oxidation of $H_2S$ to elemental sulfur on $TiO_2$ supported $V_2O_5$ catalysts. *J. Environ. Chem. Eng.* **2018**, *6*, 1414–1423. [CrossRef]
2. Yang, C.; Ye, H.; Byun, J.; Hou, Y.; Wang, X. N-Rich Carbon Catalysts with Economic Feasibility for the Selective Oxidation of Hydrogen Sulfide to Sulfur. *Environ. Sci. Technol.* **2020**, *54*, 12621–12630. [CrossRef]
3. Wiheeb, A.D.; Shamsudin, I.K.; Ahmad, M.A.; Murat, M.N.; Kim, J.; Othman, M.R. Present technologies for hydrogen sulfide removal from gaseous mixtures. *Rev. Chem. Eng.* **2013**, *29*, 449–470. [CrossRef]
4. Garcia-Arriaga, V.; Alvarez-Ramirez, J.; Amaya, M.; Sosa, E. $H_2S$ and $O_2$ influence on the corrosion of carbon steel immersed in a solution containing 3 M diethanolamine. *Corros. Sci.* **2010**, *52*, 2268–2279. [CrossRef]
5. Hao, Z. $H_2S$ selective catalytic oxidation: Catalysts and processes. *ACS Catal.* **2015**, *5*, 1053–1067.
6. Huang, H.; Shen, L.; Yang, S.; Hu, W.; Zhang, L.; Feng, J.; Jiang, L.; Yu, T.; Li, Z.; Zou, Z. Exploring N-Containing Compound Catalyst for $H_2S$ Selective Oxidation: Case Study of TaON and $Ta_3N_5$. *Catal. Lett.* **2021**, *151*, 1728–1737. [CrossRef]
7. Liu, Y.; Song, C.; Wang, Y.; Cao, W.; Lei, Y.; Feng, Q.; Chen, Z.; Liang, S.; Xu, L.; Jiang, L. Rational designed Co@ N-doped carbon catalyst for high-efficient $H_2S$ selective oxidation by regulating electronic structures. *Chem. Eng. J.* **2020**, *401*, 126038. [CrossRef]

8. Fang, H.-B.; Zhao, J.-T.; Fang, Y.-T.; Huang, J.-J.; Wang, Y. Selective oxidation of hydrogen sulfide to sulfur over activated carbon-supported metal oxides. *Fuel* **2013**, *108*, 143–148. [CrossRef]
9. Ba, H.; Duong-Viet, C.; Liu, Y.; Nhut, J.-M.; Granger, P.; Ledoux, M.J.; Pham-Huu, C. Nitrogen-doped carbon nanotube spheres as metal-free catalysts for the partial oxidation of $H_2S$. *Comptes Rendus Chim.* **2016**, *19*, 1303–1309. [CrossRef]
10. Bineesh, K.V.; Kim, D.-K.; Kim, D.-W.; Cho, H.-J.; Park, D.-W. Selective catalytic oxidation of $H_2S$ to elemental sulfur over $V_2O_5$/Zr-pillared montmorillonite clay. *Energy Environ. Sci.* **2010**, *3*, 302–310. [CrossRef]
11. Soriano, M.; Nieto, J.L.; Ivars, F.; Concepcion, P.; Rodríguez-Castellón, E. Alkali-promoted $V_2O_5$ catalysts for the partial oxidation of $H_2S$ to sulphur. *Catal. Today* **2012**, *192*, 28–35. [CrossRef]
12. Phatyenchuen, S.; Pongthawornsakun, B.; Panpranot, J.; Praserthdam, P. Effect of transition metal dopants (M= Nb, La, Zr, and Y) on the M-$TiO_2$ supported $V_2O_5$ catalysts in the selective oxidation of $H_2S$ to elemental sulfur. *J. Environ. Chem. Eng.* **2018**, *6*, 5655–5661. [CrossRef]
13. Daraee, M.; Baniadam, M.; Rashidi, A.; Maghrebi, M. Synthesis of $TiO_2$-CNT hybrid nanocatalyst and its application in direct oxidation of $H_2S$ to S. *Chem. Phys.* **2018**, *511*, 7–19. [CrossRef]
14. Ghasemy, E.; Emrooz, H.B.M.; Rashidi, A.; Hamzehlouyan, T. Highly uniform molybdenum oxide loaded N-CNT as a remarkably active and selective nanocatalyst for $H_2S$ selective oxidation. *Sci. Total. Environ.* **2020**, *711*, 134819. [CrossRef] [PubMed]
15. Varandili, S.B.; Babaei, A.; Ataie, A. Characterization of B site codoped $LaFeO_3$ nanoparticles prepared via co-precipitation route. *Rare Met.* **2018**, *37*, 181–190. [CrossRef]
16. Wang, G.; Cheng, C.; Zhu, J.; Wang, L.; Gao, S.; Xia, X. Enhanced degradation of atrazine by nanoscale $LaFe_{1-x}Cu_xO_{3-\delta}$ perovskite activated peroxymonosulfate: Performance and mechanism. *Sci. Total. Environ.* **2019**, *673*, 565–575. [CrossRef]
17. Madoui, N.; Omari, M. Synthesis and electrochemical properties of $LaCr_{1-x}Co_xO3$ ($0 \leq x \leq 0.5$) via co-precipitation method. *J. Inorg. Organomet. Polym. Mater.* **2016**, *26*, 1005–1013. [CrossRef]
18. Pena, M.; Fierro, J. Chemical structures and performance of perovskite oxides. *Chem. Rev.* **2001**, *101*, 1981–2018. [CrossRef]
19. Omari, E.; Omari, M.; Barkat, D. Oxygen evolution reaction over copper and zinc co-doped $LaFeO_3$ perovskite oxides. *Polyhedron* **2018**, *156*, 116–122. [CrossRef]
20. Da, Y.; Lirong, Z.; Caiyun, W.; Teng, M.; Rui, C.; Cairong, G.; Guoliang, F. Catalytic Oxidation of diesel soot particulates over Pt substituted $LaMn_{1-x}Pt_xO_3$ perovskite oxides. *Catal. Today* **2019**, *327*, 73–80. [CrossRef]
21. Wang, S.; Xu, X.; Zhu, J.; Tang, D.; Zhao, Z. Effect of preparation method on physicochemical properties and catalytic performances of $LaCoO_3$ perovskite for CO oxidation. *J. Rare Earths* **2019**, *37*, 970–977. [CrossRef]
22. Zhou, C.; Feng, Z.; Zhang, Y.; Hu, L.; Chen, R.; Shan, B.; Yin, H.; Wang, W.G.; Huang, A. Enhanced catalytic activity for NO oxidation over Ba doped $LaCoO_3$ catalyst. *RSC Adv.* **2015**, *5*, 28054–28059. [CrossRef]
23. Yang, X.; Park, D.-W.; Kim, M.-I. Selective oxidation of hydrogen sulfide over $LaCoO_3$ and $LaSrCoO_4$ mixed oxides. *Korean J. Chem. Eng.* **2007**, *24*, 592–595. [CrossRef]
24. Zhang, F.; Zhang, X.; Jiang, G.; Li, N.; Hao, Z.; Qu, S. $H_2S$ selective catalytic oxidation over Ce substituted $La_{1-x}Ce_xFeO_3$ perovskite oxides catalyst. *Chem. Eng. J.* **2018**, *348*, 831–839. [CrossRef]
25. Ahmad, A.; Al Mamun, M.; Al-Mamun, M.; Huque, S.; Ismail, M. LFO Perovskites as Oxygen Carriers for Chemical Looping Oxygen Uncoupling (CLOU). *J. Therm. Anal. Calorim.* **2021**, 1–9. [CrossRef]
26. Zhang, F.; Zhang, X.; Jiang, G.; Sun, Y.; Qu, S. Selective oxidation of $H_2S$ over Fe supported on Zr-intercalated Laponite clay mesoporous composite catalysts at low temperature. *Catal. Today* **2020**, *355*, 366–374. [CrossRef]
27. Xin, Z.; Zhuo, W.; Tang, Y.; Qiao, N.; Hao, Z. Catalytic Behaviors of Combined Oxides Derived from Mg/$Al_xFe_{1-x}$-Cl Layered Double Hydroxides for $H_2S$ Selective Oxidation. *Catal. Sci. Technol.* **2015**, *5*, 4991–4999.
28. Gaikwad, V.M.; Sheikh, J.R.; Acharya, S.A. Investigation of photocatalytic and dielectric behavior of $LaFeO_3$ nanoparticles prepared by microwave-assisted sol–gel combustion route. *J. Sol-Gel Sci. Technol.* **2015**, *76*, 27–35. [CrossRef]
29. Andoulsi, R.; Horchani-Naifer, K.; Férid, M. Effect of the preparation route on the structure and microstructure of $LaCoO_3$. *Chem. Pap.* **2014**, *68*, 608–613. [CrossRef]
30. Chumakova, V.; Marikutsa, A.; Rumyantseva, M.; Fasquelle, D.; Gaskov, A. Nanocrystalline $LaCoO_3$ modified by Ag nanoparticles with improved sensitivity to $H_2S$. *Sens. Actuators B Chem.* **2019**, *296*, 126661. [CrossRef]
31. Sarker, A.R. Synthesis of high quality $LaCoO_3$ crystals using water based sol-gel method. *Int. J. Mater. Sci. Appl.* **2015**, *4*, 159–164.
32. Noroozifar, M.; Khorasani-Motlagh, M.; Ekrami-Kakhki, M.-S.; Khaleghian-Moghadam, R. Enhanced electrocatalytic properties of Pt–chitosan nanocomposite for direct methanol fuel cell by $LaFeO_3$ and carbon nanotube. *J. Power Sources* **2014**, *248*, 130–139. [CrossRef]
33. Li, J.; Pan, X.; Xu, Y.; Jia, L.; Yi, X.; Fang, W. Synergetic effect of copper species as cocatalyst on $LaFeO_3$ for enhanced visible-light photocatalytic hydrogen evolution. *Int. J. Hydrogen Energy* **2015**, *40*, 13918–13925. [CrossRef]
34. Merino, N.A.; Barbero, B.P.; Grange, P.; Cadús, L.E. $La_{1-x}Ca_xCoO_3$ perovskite-type oxides: Preparation, characterisation, stability, and catalytic potentiality for the total oxidation of propane. *J. Catal.* **2005**, *231*, 232–244. [CrossRef]
35. Zhou, C.; Liu, X.; Wu, C.; Wen, Y.; Xue, Y.; Chen, R.; Zhang, Z.; Shan, B.; Yin, H.; Wang, W.G. NO oxidation catalysis on copper doped hexagonal phase $LaCoO_3$: A combined experimental and theoretical study. *Phys. Chem. Chem. Phys.* **2014**, *16*, 5106–5112. [CrossRef] [PubMed]
36. Wachowski, L.; Zielinski, S.; Burewicz, A. Preparation, stability and oxygen stoichiometry in perovskite-type binary oxides. *Acta Chim. Acad. Sci. Hung.* **1981**, *106*, 217–225.

37. Zheng, X.; Li, Y.; You, W.; Lei, G.; Cao, Y.; Zhang, Y.; Jiang, L. Construction of Fe-doped $TiO_{2-x}$ ultrathin nanosheets with rich oxygen vacancies for highly efficient oxidation of $H_2S$. *Chem. Eng. J.* **2022**, *430*, 132917. [CrossRef]
38. Zheng, X.; Li, Y.; Zheng, Y.; Shen, L.; Xiao, Y.; Cao, Y.; Zhang, Y.; Au, C.; Jiang, L. Highly Efficient Porous $Fe_xCe_{1-x}O_{2-\delta}$ with Three-Dimensional Hierarchical Nanoflower Morphology for $H_2S$-Selective Oxidation. *ACS Catal.* **2020**, *10*, 3968–3983. [CrossRef]
39. Merino, N.A.; Barbero, B.P.; Ruiz, P.; Cadús, L.E. Synthesis, characterisation, catalytic activity and structural stability of $LaCo_{1-y}Fe_yO_{3\pm\lambda}$ perovskite catalysts for combustion of ethanol and propane. *J. Catal.* **2006**, *240*, 245–257. [CrossRef]
40. Escalona, N.; Fuentealba, S.; Pecchi, G. Fischer–Tropsch synthesis over $LaFe_{1-x}Co_xO_3$ perovskites from a simulated biosyngas feed. *Appl. Catal. A Gen.* **2010**, *381*, 253–260. [CrossRef]
41. Yu, S.; Xu, S.; Sun, B.; Lu, Y.; Li, L.; Zou, W.; Wang, P.; Gao, F.; Tang, C.; Dong, L. Synthesis of $CrO_x$/C catalysts for low temperature $NH_3$-SCR with enhanced regeneration ability in the presence of $SO_2$. *RSC Adv.* **2018**, *8*, 3858–3868. [CrossRef]
42. Deng, H.B.; Gao, L.; Long, Z.; Liu, D.T.; Lin, L. Studies on catalysis of Cu-doped Mn-based perovskite-type oxide in wet oxidation of lignin to produce aromatic aldehydes. *Energy Fuels* **2010**, *24*, 4797–4802. [CrossRef]
43. Ding, J.C.; Li, H.Y.; Cai, Z.X.; Wang, X.X.; Guo, X. Near room temperature CO sensing by mesoporous $LaCoO_3$ nanowires functionalized with Pd nanodots. *Sens. Actuators B Chem.* **2016**, *222*, 517–524. [CrossRef]
44. Liu, H.; Sun, H.; Xie, R.; Zhang, X.; Zheng, K.; Peng, T.; Wu, X.; Zhang, Y. Substrate-dependent structural and CO sensing properties of $LaCoO_3$ epitaxial films. *Appl. Surf. Sci.* **2018**, *442*, 742–749. [CrossRef]
45. Koyuncu, D.D.E.; Yasyerli, S. Selectivity and Stability Enhancement of Iron Oxide Catalyst by Ceria Incorporation for Selective Oxidation of $H_2S$ to Sulfur. *Ind. Eng. Chem. Res.* **2009**, *48*, 5223–5229. [CrossRef]
46. Yong, Z.; Jiang, B.; Yuan, M.; Li, P.; Wei, L.; Zheng, X. Formaldehyde-sensing properties of $LaFeO_3$ particles synthesized by citrate sol–gel method. *J. Sol-Gel Sci. Technol.* **2016**, *79*, 167–175.
47. Bhargav, K.K.; Maity, A.; Ram, S.; Majumder, S.B. Low temperature butane sensing using catalytic nano-crystalline lanthanum ferrite sensing element. *Sens. Actuators B Chem.* **2014**, *195*, 303–312. [CrossRef]
48. Lee, W.Y.; Yun, H.J.; Yoon, J.W. Characterization and magnetic properties of $LaFeO_3$ nanofibers synthesized by electrospinning. *J. Alloy. Compd.* **2014**, *583*, 320–324. [CrossRef]
49. Barbero, B.P.; Gamboa, J.A.; Cadús, L.E. Synthesis and characterisation of La1xCaxFeO3 perovskite-type oxide catalysts for total oxidation of volatile organic compounds. *Appl. Catal. B Environ.* **2006**, *65*, 21–30. [CrossRef]
50. Li, M.; Gao, Y.; Zhao, K.; Li, H.; Huang, Z. Mg-doped $La_{1.6}Sr_{0.4}FeCoO_6$ for anaerobic oxidative dehydrogenation of ethane using surface-absorbed oxygen with tuned electronic structure. *Fuel Process. Technol.* **2021**, *216*, 106771. [CrossRef]
51. Zhang, F.; Zhang, X.; Hao, Z.; Jiang, G.; Yang, H.; Qu, S. Insight into the $H_2S$ selective catalytic oxidation performance on well-mixed Ce-containing rare earth catalysts derived from MgAlCe layered double hydroxides. *J. Hazard. Mater.* **2018**, *342*, 749–757. [CrossRef] [PubMed]
52. Cantrell, K.J.; Yabusaki, S.B.; Engelhard, M.H.; Mitroshkov, A.V.; Thornton, E.C. Oxidation of $H_2S$ by iron oxides in unsaturated conditions. *Environ. Sci. Technol.* **2003**, *37*, 2192–2199. [CrossRef] [PubMed]